JM PAPERS

Analytical models for pressure-driven Stokes flow through superhydrophobic and liquid-infused tubes and annular pipes*

Sebastian Zimmermann[1] and Clarissa Schönecker[1,2],†

[1]Department of Mechanical and Process Engineering, Rheinland-Pfälzische Technische Universität Kaiserslautern-Landau (RPTU), D-67663 Kaiserslautern, Germany

[2]Max Planck Institute for Polymer Research, Mainz, Germany

Analytical expressions for the velocity field and the effective slip length of pressure-driven Stokes flow through slippery pipes and annuli with rotationally symmetrical longitudinal slits are derived. Specifically, the developed models incorporate a finite local slip length and constant shear stress along the slits, and thus go beyond the assumption of perfect slip employed commonly for superhydrophobic surfaces. Thereby, they provide the possibility to assess the influence of both the viscosity of the air or other fluid that is modelled to fill the slits as well as the influence of the micro-geometry of these slits. First, expressions for tubes and annular pipes with superhydrophobic or slippery walls are provided. Second, these solutions are combined to a tube-within-a circular-pipe scenario, where one fluid domain provides a slip to the other. This scenario is interesting as an application to achieve stable fluid–fluid interfaces. With respect to modelling, it illustrates the specification of the local slip length depending on a linked flow field. The comparison of the analytically calculated solutions with numerical simulations shows excellent agreement. The results of this paper thus represent an important instrument for the design and optimization of slippage along surfaces in circular geometries.

Key words: low-Reynolds-number flows, micro-/nano-fluid dynamics

1. Introduction

Flows over microstructured or nanostructured surfaces are of great technical importance. For example, grooves, posts or holes are incorporated into no-slip walls whose structures

† Email address for correspondence: c.schoenecker@mv.rptu.de
* Article updated 07 February 2024.

contain a secondary immiscible fluid, as in the case of superhydrophobic surfaces (Shirtcliffe *et al.* 2010), where air is trapped between the primary water flow and the wall structuring. This wetting scenario is called the Cassie state, where the primary fluid wets only the upper surface of the structure, forming a heterogeneous solid–liquid and solid–gas interface (Cassie & Baxter 1944). Such configurations lead to a lower surface wettability and thus to self-cleaning and water-repellent behaviour as for the lotus leaf (Koch, Bhushan & Barthlott 2009). Furthermore, the relative surface fraction of the no-slip wall is reduced, and the primary fluid can slide over air cushions on the surface, reducing drag significantly (Vinogradova 1999; Ou, Perot & Rothstein 2004; Belyaev & Vinogradova 2010; Rothstein 2010; Karatay *et al.* 2013). This is of great importance since hydrodynamic drag is related directly to the energy required to transport a fluid through a domain bounded by walls, implying a potential high economic incentive. The reduction in drag is caused by the ability of the primary flow to exhibit a finite velocity on the fluid–fluid interface in comparison to a solid wall. This induces an internal movement and potentially results in circulation of the fluid trapped within the microtexture. Depending on the internal resistance of the fluid to displacement, the primary flow experiences drag (McHale, Flynn & Newton 2011). Air is therefore a suitable secondary fluid due to its low viscosity. However, a key factor is the ability of the interface to shift according to the experienced shear stress. This mobility can be limited by deposited surfactants and impurities (Schäffel *et al.* 2016). The interface then becomes rigid, and circulation within the textures is no longer possible (McHale *et al.* 2011). Additionally, air dissipation from the microstructures can occur (Nizkaya, Asmolov & Vinogradova 2014). The interface then migrates into the microstructure (sagging) and drives the remaining air out, i.e. the primary fluid has conquered and filled all microstructures. The result for both cases is the Wenzel state (Wenzel 1936). The slipping effect is then reduced significantly. Surfaces impregnated with a lubricant instead of air (liquid-infused surfaces) have proven to be a useful tool to prevent such Cassie–Wenzel transitions (Wong *et al.* 2011) while still allowing slippage (Asmolov, Nizkaya & Vinogradova 2018), and are therefore receiving increasing attention (Hardt & McHale 2022). Liquid-infused surfaces promote anti-icing (Latthe *et al.* 2019) and anti-biofouling (Epstein *et al.* 2012) effects, which are major challenges in various industries such as transportation, agriculture and energy (Cao *et al.* 2009; Ras & Marmur 2016; Agbe, Sarkar & Chen 2020).

To maximize the area fraction of the secondary fluid and to account for possible interface collapse, numerous microstructures are incorporated onto the surface. Since these are much smaller than the general geometry, complete numerical resolution of the full domain is not feasible. One way to solve this problem is to average the cumulative effect of all microstructures across the patterned wall and implement it into the numerical model using the Navier-slip boundary condition

$$w = \lambda_{eff} \frac{\partial w}{\partial \boldsymbol{n}}. \tag{1.1}$$

The effective slip length λ_{eff} can be understood as a virtual depth below the surface where the velocity is extrapolated to zero (see figure 1) and connects the velocity w with its normal derivative on the slip wall. Thus it is an important input quantity for numerical studies of microstructured surfaces, and can be extracted from analytical models. Superhydrophobic structures of particular importance for application are parallel longitudinal stripes on pipe surfaces (see figure 3 below). An important result on this subject is given by Philip (1972*a*), who derived an analytical solution for the pressure-driven flow field of a pipe containing N rotationally symmetric no-shear wall
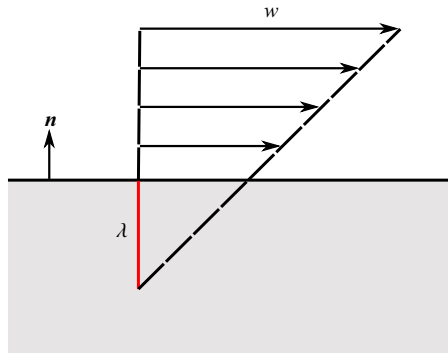
Figure 1. Schematic illustration of the slip boundary condition.

sections on an otherwise no-slip wall. Lauga & Stone (2003) took up that formula and derived the effective slip length for such a configuration using (Philip 1972*b*)

$$\tilde{\lambda}_{eff} = \frac{\lambda_{eff}}{R_0} = \frac{2}{N} \ln\left(\sec\left(\frac{\theta}{2}\right)\right), \tag{1.2}$$

with the pipe radius R_0, number of no-shear slits N, and the angle θ as a measure for the no-shear fraction with θ/π being the proportion of the total wall surface occupied by no-shear slits. Crowdy (2021) derives, among other things, analytical solutions for the effective slip length of pressure-driven annular flows containing longitudinal stripes on the inner or outer wall. In the case of stripes on the inner wall, it is given by

$$\tilde{\lambda}_{eff} = \tilde{R}_1 \ln(\tilde{R}_1) - 2\tilde{R}_1 \frac{S}{I_{-1}}, \tag{1.3}$$

with $\tilde{\lambda}_{eff}, \tilde{R}_1$ in (1.3) being normalized with respect to the outer radius of the annulus. Here, $\tilde{R}_1$ denotes the dimensionless inner radius of the annulus. The outer wall is set to be the unit disk. Also, S is a scaling constant, and I_{-1} is the coefficient in a Laurent expansion performed by Crowdy (2021), both dependent solely on geometric parameters. For further details, see § 2.2.3. However, both approaches assume perfect local slip along certain boundary parts, i.e. the primary flow experiences no shear stress there. At this point, it seems appropriate to explain the difference between molecular (or intrinsic) and apparent slip (Lauga, Brenner & Stone 2005). The former describes slippage at a molecular level, where liquid molecules actually slide along a solid wall, with the slip length amounting to a few nanometres. The latter is caused, as mentioned above, by the presence of an enclosed secondary fluid, which leads to a slip length of the order of magnitude of the surface structures. Here, the scale of the microstructures is assumed to be significantly larger than any molecular slippage (Schönecker, Baier & Hardt 2014). For this reason, the effects of the molecular slip are neglected in the following considerations.

A perfect slippage, of course, cannot be achieved in reality, but represents an ideal limit where the enclosed fluid is decoupled from the bulk flow. The local slip length is infinite. Thus in such models, it does not matter whether the microstructures are impregnated by air, oil or water – the effect remains unchanged. In addition to the viscous interaction of both fluids, the influence of the microstructure geometry is also not considered, although it plays a crucial role (see Schönecker & Hardt 2013, 2015). In other words, the drag reduction and the effective slip length are influenced strongly by the assumptions made

for the flow of the secondary fluid, restricted by the microstructure design. For example, with open longitudinal grooves, recirculation of the enclosed fluid does not necessarily occur. In closed microstructures, however, this is inevitable due to mass conservation. Furthermore, both fluids can be driven by their own pressure gradient, which, depending on the configuration, increases significantly the effective sliding length (Busse *et al.* 2013). Such a case is discussed in § 3. Therefore, it is of utmost importance to develop models that take these multiple influencing factors duly into account.

This work derives analytical equations for pressure-driven pipe flow through tubes and annuli that have rotationally symmetric slits on their walls. Such circular geometries are ubiquitous in practical applications, hence a possible control of drag reduction is highly attractive. Overall, new models for three types of geometries are derived. In the first two, pipe (§ 2.1) and annular pipe (§ 2.2) flows, the influence of the enclosed fluid on the bulk flow is modelled classically though a slip boundary condition that is applied locally at the fluid–fluid interfaces. As a novelty, the slip length at the fluid–fluid interfaces is allowed to be finite. Thereby, these solutions provide the platform to incorporate effects of the viscosity of the lubricating fluid as well as of the geometry of the microstructures. The third geometry considered is a pipe within an annular tube (§ 3). This geometry represents a fundamental implementation of how superhydrophobic or liquid-infused pipes can be realized in practice. By combining the previous two models, a full description of the flow is obtained. This means that model parameters like a slip length on the fluid–fluid boundaries are no longer required. The effect of the viscosity of the secondary fluid and the geometry of its boundaries on the flow of the primary fluid are incorporated directly. With respect to the mathematical methodology, a superposition approach is employed, which is both convenient and leads to a distribution of the local slip length that is more physical than classic assumptions of a constant local slip length, especially for high-viscosity lubricating fluids. For that, available pre-existing no-shear velocity fields, which describe the absence of shear stress at the boundary slit parts, are superposed with suitable solutions of the Poisson equation exhibiting a constant shear stress along the same boundaries. The resulting superposed velocity fields then feature constant non-zero shear stresses along these very interfaces. Finally, the results of this work are discussed, analysed and illustrated in § 4.

2. Mathematical description of the flow field and effective slip length

A pressure-driven Stokes flow $(0, 0, w(x, y))$ of a fluid of viscosity μ along the Z axis of an arbitrary Cartesian domain (x, y, Z) having a cross-section in the (x, y) plane is governed by the Poisson equation

$$\nabla^2 w(x, y) = -\frac{s}{\mu},\tag{2.1}$$

where $-s$ is the negative pressure gradient along the Z axis, and ∇ is the nabla operator in

$$\nabla^2 = \frac{\partial^2}{\partial x^2} + \frac{\partial^2}{\partial y^2}.\tag{2.2}$$

It is assumed that the Reynolds number is sufficiently small to neglect inertial forces acting on the fluid. Velocities are non-dimensionalized with respect to sL^2/μ, with L being a characteristic length of the respective flow regime. Furthermore, the finite slip boundaries follow the shape given by the pipe geometry. That is, the surface tension is large enough to prevent further curvature of the interface.
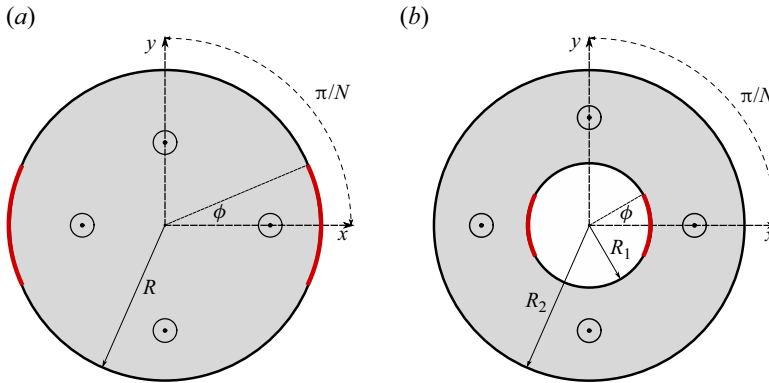
Figure 2. Liquid-infused pipes with mixed boundary conditions, no-shear (or finite constant shear) slits shown as red bold line segments along the otherwise no-slip boundaries. (*a*) Pipe flow with $N = 2$. (*b*) Annular pipe flow with $N = 2$ slits on the inner wall.

Due to the linearity of the Poisson equation, the resulting velocity field is also linear under consideration of appropriate boundary conditions. Thus flow fields can be superposed, and the result is also a linear solution of the governing partial differential equation. Consider

$$\mu \nabla^2 w_1 + \mu \nabla^2 w_2 = \nabla p_1 + \nabla p_2, \tag{2.3}$$

with additivity $f(x_1) + f(x_2) = f(x_1 + x_2)$ yielding

$$\mu \nabla^2 (w_1 + w_2) = \nabla (p_1 + p_2), \tag{2.4}$$

with the superposed velocity field $w = w_1 + w_2$ and pressure gradient $p = p_1 + p_2$. With this method, previous no-shear solutions will be extended in such a way that they possess a finite local slip length instead of an infinite one along their interface.

2.1. *Liquid-infused pipe with patterned wall*

A flow in a circular tube with N longitudinal rotationally symmetric slits on the outer wall is considered first, as illustrated in figure 2(*a*), where $N \geq 1$ is an integer.

2.1.1. *Velocity field – no-shear solution*

A very important theoretical reference for modelling superhydrophobic or slippery surfaces is Philip (1972*a*). He offers analytical solutions to a variety of mixed value boundary problems that are composed of a mixture of no-shear and no-slip boundaries. One of these solutions describes the aforementioned circular tube with longitudinal no-shear slits on the outer wall, which will be referred to as Philip pipe flow hereafter. The velocity field for an arbitrary dimensionless pipe radius $0 < |\tilde{z}| \leq \tilde{R}$ can be written as (Lauga & Stone 2003)

$$w_{pc}(\tilde{z}) = \frac{sR_0^2}{\mu} \left(\frac{1}{4} (\tilde{R}^2 - |\tilde{z}|^2) + \frac{1}{N} \tilde{R}^2 \, \tau(\tilde{z}) \right), \tag{2.5}$$

where R_0 is the dimensionally dependent pipe radius, $\tilde{R} = R/R_0$ is the normalized outer pipe radius, and $\tilde{z} = z/R_0 = \tilde{x} + i\tilde{y}$ is the dimensionless complex coordinate. The index pc indicates the circular Philip solution. It consists of a rotationally axisymmetric Poiseuille

flow superposed on an asymmetric second part with $\tau(\tilde{z})$ governing the no-shear slit influence on the flow, given by

$$\tau(\tilde{z}) = \mathrm{Im}\left[\cos^{-1}\left(\frac{\cos(\kappa(\tilde{z}))}{\cos\left(\dfrac{\theta}{2}\right)}\right) - \kappa(\tilde{z})\right] \tag{2.6}$$

and

$$\kappa(\tilde{z}) = -\frac{\mathrm{i}}{2}\ln\left(\frac{\zeta}{\tilde{R}^N}\right) = -\frac{\mathrm{i}}{2}\ln\left(\frac{\tilde{z}^N}{\tilde{R}^N}\right) = -\frac{\mathrm{i}N}{2}\ln\left(\frac{\tilde{z}}{\tilde{R}}\right). \tag{2.7}$$

Here, $\zeta = \tilde{z}^N$ is the transformed coordinate as a result of the conformal mapping performed by Philip, and Im denotes the imaginary part of an expression. As in § 1, $\theta = N\phi$ is a measure for the no-shear fraction, with ϕ being the slit half-angle.

2.1.2. *Velocity field – finite shear solution*

The Philip pipe flow solution has perfect slip along the fluid–fluid interfaces, resulting in an infinite local slip length. As mentioned, this assumption corresponds to an ideal state of fluid–fluid interaction, non-existent in reality (Bolognesi, Cottin-Bizonne & Pirat 2014). To close this gap, one needs to find a solution with finite slip along the slit parts of the boundary. Such a flow field can be described by a superposition ansatz (Schönecker *et al.* 2014)

$$w(\tilde{z}) = A_1 w_1(\tilde{z}) + A_2 w_2(\tilde{z}), \tag{2.8}$$

with $w_1(\tilde{z})$ being the aforementioned Philip pipe flow solution $w_{pc}(\tilde{z})$. The underlying assumption of this model, as mentioned before, is that the shear stress across the fluid–fluid interface is constant. To account for that, $w_2(\tilde{z})$ is chosen to be Poiseuille flow

$$w_2(\tilde{z}) = \frac{1}{4}\frac{s_2 R_0^2}{\mu}(\tilde{R}^2 - |\tilde{z}|^2). \tag{2.9}$$

The superposition ansatz thus gives

$$w(\tilde{z}) = A_1\frac{1}{4}\frac{s_1 R_0^2}{\mu}\left((\tilde{R}^2 - |\tilde{z}|^2) + \frac{\tilde{R}^2}{N}\tau(\tilde{z})\right) + A_2\frac{1}{4}\frac{s_2 R_0^2}{\mu}(\tilde{R}^2 - |\tilde{z}|^2), \tag{2.10}$$

with constants A_1 and A_2 to be determined. Note that w_1 and w_2 are driven by (different) pressure gradients s_1 and s_2, respectively. Under the condition that the combined flow is driven by a combined pressure gradient

$$s = A_1 s_1 + A_2 s_2, \tag{2.11}$$

and that the Navier-slip condition applies in the centre of the slit at $\tilde{\mathfrak{z}} = \tilde{R} + \mathrm{i}0$,

$$w(\tilde{\mathfrak{z}}) = \lambda\frac{\partial w(\tilde{\mathfrak{z}})}{-\partial\boldsymbol{n}}, \tag{2.12}$$

the constants A_1 and A_2 are readily determined. The resulting superposed velocity field solution is

$$w(\tilde{z}) = \frac{s R_0^2}{\mu}\left(\frac{1}{4}(\tilde{R}^2 - |\tilde{z}|^2) + \alpha\frac{\tilde{R}^2}{N}\tau(\tilde{z})\right), \tag{2.13}$$

normalized as

$$\tilde{w}(\tilde{z}) = w(\tilde{z}) \left(\frac{sR_0^2}{\mu}\right)^{-1} = \frac{1}{4} (\tilde{R}^2 - |\tilde{z}|^2) + \alpha \frac{\tilde{R}^2}{N} \tau(\tilde{z}), \qquad (2.14)$$

with

$$\alpha = \frac{\tilde{\lambda}N}{\tilde{\lambda}N + 2\tilde{R}\,\tau(\tilde{\mathfrak{z}})}, \qquad (2.15)$$

where $\tilde{\lambda} = \lambda/R_0$ is the dimensionless local slip length at the slit centre, and

$$\tau(\tilde{R} + \mathrm{i}0) = \tau(\tilde{\mathfrak{z}}) = \cosh^{-1}\left(\sec\left(\frac{\theta}{2}\right)\right). \qquad (2.16)$$

By comparing the superposed flow field with Philip pipe flow, we find that the solutions differ only by the coefficient α in the second term. As $\tilde{\lambda} \to \infty$, α converges to 1, and $w(\tilde{z}) \to w_{pc}(\tilde{z})$, yielding the no-shear solution, as it should. Therefore, α can be interpreted as an imperfection coefficient adjusting the slit influence on the velocity field depending on a potentially finite local slip length.

2.1.3. *Effective slip length*

With the flow field dependence on a local slip length at hand, it is now possible to calculate the effective slip length. It represents the averaged influence of the slip boundary parts on the velocity field, and involves equating the total volume flux $\dot{V}$ caused by a given pressure gradient to that of a suitable comparison flow $(0, 0, w^*(x, y))$ with the same pressure gradient, containing a no-slip wall at $|z| = R$. The effective slip length is the value of λ_{eff}, for which $\dot{V}^* = \dot{V}(\lambda_{eff})$. In our case, however, it is not necessary to calculate the volume flow. Instead, we consider a pressure-driven pipe flow with some constant effective slip length λ_{eff} at the outer wall. This will provide a simple formula that can be used to calculate the effective slip length. First, a general axisymmetrical pipe flow solution is given by

$$w^* = -\frac{s}{4\mu} |z|^2 + c_1 \ln(|z|) + c_2, \qquad (2.17)$$

subject to

$$\frac{\partial w^*(|z| = 0)}{\partial |z|} = 0, \quad w^*(|z| = R) = \lambda_{eff} \frac{\partial w^*(|z| = R)}{-\partial |z|}, \qquad (2.18a,b)$$

which yields

$$w^* = \frac{1}{4} \frac{s}{\mu} (R^2 - |z|^2) + \frac{1}{2} \frac{s}{\mu} R\lambda_{eff}, \qquad (2.19)$$

which corresponds to a pipe flow with constant slip λ_{eff} at the outer wall. This can be interpreted as the effective slip length. From (2.19), an expression for λ_{eff} at $|z| = R$ is

determined easily to be

$$\lambda_{eff} = \frac{\mu}{s} \frac{2}{R} w^*(R). \tag{2.20}$$

As mentioned above, all groove influence is abstracted to an average effect on the given wall. So all that is left to do is to average (2.13) along the boundary

$$w^*(R) = \frac{1}{2\pi} \int_0^{2\pi} w(R) \, \mathrm{d}\varphi = \alpha \frac{s}{\mu} \frac{R^2}{N} \frac{1}{2\pi} \int_0^{2\pi} \tau(\tilde{z}) \, \mathrm{d}\varphi, \tag{2.21}$$

where φ is the coordinate angle. Solving the above integral involves using the integral relation derived by Philip (1972b), stating that the averaged slip influence is given by

$$\frac{1}{2\pi} \int_0^{2\pi} \tau(\tilde{z}) \, \mathrm{d}\varphi = \bar{\tau}(\tilde{z}) = \ln\left(\sec\left(\frac{\theta}{2}\right)\right). \tag{2.22}$$

The resulting normalized effective slip length $\tilde{\lambda}_{eff} = \lambda_{eff}/R$ is

$$\tilde{\lambda}_{eff} = \alpha \frac{2}{N} \ln\left(\sec\left(\frac{\theta}{2}\right)\right). \tag{2.23}$$

Equation (2.23) again transitions into the Philip solution if the local slip length diverges. However, there is a more straightforward way to calculate the effective slip length. Equation (2.20) shows that the Poiseuille part is not contributing to the effective slip length, since it is zero at $|z| = R$, while the second part is non-zero on the boundary and contributes with the factor α. The normalized slip length can therefore be determined directly by

$$\tilde{\lambda}_{eff} = \alpha \tilde{\lambda}_{eff,P}, \tag{2.24}$$

with $\tilde{\lambda}_{eff,P}$ being the effective slip length of the Philip (1972a) no-shear solution.

2.1.4. *Volume flow*

Another useful result is the total volume flux generated by the superposed flow of (2.13). For this purpose, we consider the volume flow to be given by

$$\dot{V} = 2\pi \int_0^R w(x, y) \, r \, \mathrm{d}r = 2 \frac{s\pi}{\mu} \int_0^R \left(\frac{1}{4}(R^2 - |z|^2) + \alpha \frac{R^2}{N} \bar{\tau}(\tilde{z})\right) r \, \mathrm{d}r, \tag{2.25}$$

where we again use the integral identity of Philip (1972b). The associated total volume flux is therefore

$$\dot{V} = \frac{s\pi}{\mu} \left(\frac{1}{8} R^4 + \alpha \frac{R^4}{N} \ln\left(\sec\left(\frac{\theta}{2}\right)\right)\right). \tag{2.26}$$

As in (2.13), with $\tilde{\lambda} \to \infty$ the volume flux transitions into the Philip solution (Philip 1972b), representing the ideal no-shear limit. With the comparison volume flux of a Poiseuille flow with no-slip at the outer wall being

$$\dot{V}_{ns} = \frac{1}{8} \frac{s\pi}{\mu} R^4, \tag{2.27}$$

the effective slip length can be calculated alternatively with

$$\lambda_{eff} = \frac{R}{4} \left(\frac{\dot{V}}{\dot{V}_{ns}} - 1\right), \tag{2.28}$$

which also results in (2.23).

978 A20-8

2.2. *Annular liquid-infused pipe with patterned inner wall*

A second flow regime of great interest is an annular slippery pipe with N rotationally symmetric slits on the inner boundary wall, as illustrated in figure 2(b).

2.2.1. *Velocity field – no-shear solution*

Crowdy (2021) provides an analytical flow field solution for annular superhydrophobic pipes of radius $\tilde{R}_1 \leq |\tilde{z}| \leq \tilde{R}_2$, with $\tilde{R}_2 = 1$, and $N \geq 1$ no-shear boundary slits on the inner wall. The velocity field is given as

$$w_{ca}(\tilde{z}) = \frac{sR_0^2}{\mu} \left(\frac{1}{4} (1 - |\tilde{z}|^2) + \frac{1}{2} \text{Re}(H(\zeta)) \right), \tag{2.29}$$

where the subscript ca indicates the Crowdy annular flow field (Crowdy 2021). Like (2.5), this solution consists of a rotationally symmetric Poiseuille flow and a superposed asymmetric second term with the real part of an analytic function $H(\zeta)$. This function represents the slit influence on the flow field and is

$$H(\zeta) = \frac{1}{N} \int_{-1}^{\zeta} \left[\tilde{R}_1^2 - M \left(\frac{P\left(\frac{\zeta'}{q}, q\right) P\left(\frac{\zeta'}{q}, q\right)}{P\left(\frac{\zeta'}{a}, q\right) P\left(\frac{\zeta'}{\bar{a}}, q\right)} \right)^{1/2} \right] \frac{\mathrm{d}\zeta'}{\zeta'}, \tag{2.30}$$

where $a = \tilde{R}_1^N e^{i\theta}$, and $q = \tilde{R}_1^N$. The angle $\theta = \phi N$ is defined in the same way as for the Philip pipe solution. The variable $\zeta = z^N$ is, as before, the transformed complex coordinate. Also, M is a scaling factor determined by imposing $w_{ca}(x, y) = 0$ on the no-slip portions of the inner wall:

$$M = \frac{\dfrac{1 - \tilde{R}_1^2}{4} + \dfrac{1}{2} \tilde{R}_1^2 \ln(\tilde{R}_1)}{S}, \tag{2.31}$$

with

$$S = \frac{1}{2N} \int_{-1}^{-q} \left(\frac{P\left(\frac{\zeta}{q}, q\right) P\left(\frac{\zeta}{q}, q\right)}{P\left(\frac{\zeta}{a}, q\right) P\left(\frac{\zeta}{\bar{a}}, q\right)} \right)^{1/2} \frac{\mathrm{d}\zeta}{\zeta}. \tag{2.32}$$

Here, $P(\zeta, q)$ is called the prime function for the concentric annulus and is defined as a convergent infinite product for any $\zeta \neq 0$:

$$P(\zeta, q) = (1 - \zeta) \prod_{n=1}^{\infty} (1 - q^{2n} \zeta)(1 - q^{2n}/\zeta), \quad 0 \leq q < 1. \tag{2.33}$$

For further information on prime functions, see Crowdy (2020).

2.2.2. *Velocity field – finite shear solution*

As for Philip pipe flow, we seek a solution that does not necessarily impose an infinite local slip length on the slit portions of the boundary, but rather has a potentially finite local slip length. As before, constant shear stress along the fluid–fluid interface is assumed. We again choose a superposition approach

$$w(\tilde{z}) = B_1 \, w_1(\tilde{z}) + B_2 \, w_2(\tilde{z}), \qquad (2.34)$$

with $w_1(\tilde{z})$ being the no-shear solution for the annulus provided by Crowdy (2021), and $w_2(\tilde{z})$ chosen to be the Poiseuille solution for an annular domain, with $w_2(\tilde{z}) = 0$ at $|\tilde{z}| = \tilde{R}_1$ and $|\tilde{z}| = 1$, resulting in

$$w_2(\tilde{z}) = \frac{1}{4} \frac{s_2 R_0^2}{\mu} \left((1 - |\tilde{z}|^2) - (1 - \tilde{R}_1^2) \frac{\ln(|\tilde{z}|)}{\ln(\tilde{R}_1)} \right). \qquad (2.35)$$

The superposition ansatz thus gives

$$w(\tilde{z}) = B_1 \frac{s_1 R_0^2}{\mu} \left(\frac{1}{4} (1 - |\tilde{z}|^2) + \frac{1}{2} \operatorname{Re}(H(\zeta)) \right)$$
$$+ B_2 \frac{1}{4} \frac{s_2 R_0^2}{\mu} \left((1 - |\tilde{z}|^2) - (1 - \tilde{R}_1^2) \frac{\ln(|\tilde{z}|)}{\ln(\tilde{R}_1)} \right), \qquad (2.36)$$

with constants B_1 and B_2 again to be determined. Here, w_1 and w_2, as before, are driven by the pressure gradients s_1 and s_2, respectively. Under the condition that the combined flow is driven by a combined pressure gradient

$$s = B_1 s_1 + B_2 s_2, \qquad (2.37)$$

and with the Navier-slip condition imposed at the centre of the slit $\tilde{\mathfrak{z}} = \tilde{R}_1 + i0$

$$w(\tilde{\mathfrak{z}}) = \lambda \frac{\partial w(\tilde{\mathfrak{z}})}{\partial \boldsymbol{n}}, \qquad (2.38)$$

the constants B_1 and B_2 are determined, yielding the corresponding superposed flow field

$$w(\tilde{z}) = \frac{1}{4} \frac{s R_0^2}{\mu} \left((1 - |\tilde{z}|^2) + 2\beta_1 \operatorname{Re}(H(\zeta)) - \beta_2 (1 - \tilde{R}_1^2) \frac{\ln(|\tilde{z}|)}{\ln(\tilde{R}_1)} \right), \qquad (2.39)$$

with

$$\beta_1 = \frac{\tilde{\lambda} \left(\tilde{R}_1^2 + 2\tilde{R}_1^2 \ln \left(\dfrac{1}{\tilde{R}_1} \right) - 1 \right)}{\tilde{R}_1^2 \tilde{\lambda} - \tilde{\lambda} + \tilde{R}_1 \ln \left(\dfrac{1}{\tilde{R}_1} \right) (\tilde{R}_1^2 - 2 \operatorname{Re}(H(q)) + 2\tilde{\lambda}\tilde{R}_1 - 1)} \qquad (2.40)$$

and

$$\beta_2 = (1 - \beta_1) = \frac{\tilde{R}_1 \ln \left(\dfrac{1}{\tilde{R}_1} \right) (\tilde{R}_1^2 - 2 \operatorname{Re}(H(q)) - 1)}{\tilde{R}_1^2 \tilde{\lambda} - \tilde{\lambda} + \tilde{R}_1 \ln \left(\dfrac{1}{\tilde{R}_1} \right) (\tilde{R}_1^2 - 2 \operatorname{Re}(H(q)) + 2\tilde{\lambda}\tilde{R}_1 - 1)}, \qquad (2.41)$$

where $\tilde{\lambda} = \lambda/R_0$ is the normalized local slip length, and $H(q)$ is the value of the analytic function $H(\zeta)$ evaluated at the centre of the slit boundary portion, at coordinate $\tilde{\mathfrak{z}}$,

corresponding to $\zeta(\tilde{\mathfrak{z}}) = q$. Analysing the behaviour of (2.39) depending on coefficients β_1 and β_2 shows that for $\tilde{\lambda} \to \infty$, $\beta_1 \to 1$ and $\beta_2 \to 0$, delivering the no-shear solution of (2.29). Therefore both coefficients can be referred to as weighting coefficients, steering the influence of the no-shear (2.29) and no-slip solution (2.35) on the superposed flow field. The normalized velocity field is calculated easily to be

$$\tilde{w}(\tilde{z}) = \frac{1}{4} \left((1 - |\tilde{z}|^2) + 2\beta_1 \operatorname{Re}(H(\zeta)) - \beta_2(1 - \tilde{R}_1^2) \frac{\ln(|\tilde{z}|)}{\ln(\tilde{R}_1)} \right). \qquad (2.42)$$

2.2.3. *Effective slip length*

As with the pipe flow in § 2.1.3, a suitable comparison flow is needed to determine the effective slip length for the superposed annular flow above. For that, the general axisymmetrical solution of (2.17) is solved again, with velocity normalized with respect to sR_0^2/μ, and length scales with R_0. This solution is subject to no-slip on the wall at $|\tilde{z}| = \tilde{R}_2 = 1$ and a Navier-slip boundary condition at $|\tilde{z}| = \tilde{R}_1$, so

$$\tilde{w}^*(|\tilde{z}| = \tilde{R}_2) = 0, \quad \tilde{w}^*(|\tilde{z}| = \tilde{R}_1) = \tilde{\lambda} \frac{\partial \tilde{w}^*(|\tilde{z}| = \tilde{R}_1)}{\partial |\tilde{z}|}. \qquad (2.43a,b)$$

Implementing both boundary conditions yields an annular axisymmetric solution with a constant slip length at $|\tilde{z}| = \tilde{R}_1$, which can be interpreted as an effective slip along that boundary $\tilde{\lambda} \equiv \tilde{\lambda}_{eff}$. The solution for the flow field is found to be

$$\tilde{w}^* = \frac{1 - |\tilde{z}|^2}{4} - \tilde{R}_1 \ln(|\tilde{z}|) \frac{\tilde{R}_1^2 - 2\tilde{R}_1\tilde{\lambda}_{eff} - 1}{4(\tilde{\lambda}_{eff} - \tilde{R}_1 \ln(\tilde{R}_1))}. \qquad (2.44)$$

Evaluating this solution at the inner slip wall $|\tilde{z}| = \tilde{R}_1$ gives

$$\tilde{w}^*(|\tilde{z}| = \tilde{R}_1) = \frac{1 - \tilde{R}_1^2}{4} - \tilde{R}_1 \ln(\tilde{R}_1) \frac{\tilde{R}_1^2 - 2\tilde{R}_1\tilde{\lambda}_{eff} - 1}{4(\tilde{\lambda}_{eff} - \tilde{R}_1 \ln(\tilde{R}_1))}. \qquad (2.45)$$

A rearrangement provides a formula for the effective slip length on the inner wall of the annulus $\tilde{R}_1 \le |\tilde{z}| \le 1$ as a function of the normalized velocity $\tilde{w}^*$ on that very wall:

$$\tilde{\lambda}_{eff} = -\frac{4\tilde{R}_1 \ln(\tilde{R}_1)\tilde{w}^*}{1 - \tilde{R}_1^2 - 4\tilde{w}^* + 2\tilde{R}_1^2 \ln(\tilde{R}_1)}. \qquad (2.46)$$

As mentioned earlier, the effective slip length abstracts the cumulative groove influence on the flow field as an average effect along the respective wall. Equation (2.42), however, is based on mixed boundary conditions along the groove containing wall. It is easy to see that the velocity is not constant, since it is zero at the no-slip portions, and non-zero along the slits. Therefore, it is necessary to average the velocity along $|\tilde{z}| = \tilde{R}_1$, and thus indirectly the groove effect. A closer look at (2.29) and (2.42) reveals that the only rotationally asymmetric terms are those containing the real part of the analytic function $H(\zeta)$. The no-shear and finite shear solutions are thus related closely with respect to their asymmetric behaviour. Therefore, it makes sense to first consider the effective slip length of the former. The finite slip solution can then be considered as a simple extension of it.

Reconstructing the effective slip length of the no-shear solution derived by Crowdy (2021), we must first identify the average of $\text{Re}(H(\zeta))$ at $|\tilde{z}| = \tilde{R}_1$ along the inner wall:

$$\text{Re}(H(\zeta))_{avg} = \frac{1}{2\pi} \int_0^{2\pi} \text{Re}(H(\zeta)) \, \mathrm{d}\varphi. \tag{2.47}$$

Although not given explicitly in Crowdy (2021), it is readily determined to be

$$\text{Re}(H(\zeta))_{avg} = \tilde{R}_1^2 \ln(\tilde{R}_1) - MI_{-1} \ln(\tilde{R}_1), \tag{2.48}$$

with the aforementioned scaling factor M from (2.31), and

$$I_{-1} = \frac{1}{2\pi \mathrm{i}} \oint_C \left(\frac{P\left(\dfrac{\zeta}{q}, q\right) P\left(\dfrac{\zeta}{q}, q\right)}{P\left(\dfrac{\zeta}{a}, q\right) P\left(\dfrac{\zeta}{\bar{a}}, q\right)} \right)^{1/2} \frac{\mathrm{d}\zeta}{\zeta}, \tag{2.49}$$

where C is any closed circle inside the annulus $q < |\zeta| < 1$ enclosing the origin (Crowdy 2021). Accordingly, the averaged velocity for the no-shear solution along the inner wall is given by

$$\tilde{w}^*_{ca}(|\tilde{z}| = \tilde{R}_1) = \tfrac{1}{4}(1 - \tilde{R}_1^2) + \tfrac{1}{2}(\tilde{R}_1^2 \ln(\tilde{R}_1) - MI_{-1} \ln(\tilde{R}_1)), \tag{2.50}$$

and the associated normalized effective slip length for the no-shear case is

$$\tilde{\lambda}_{eff,ca} = \frac{\lambda_{eff,ca}}{R_0} = \tilde{R}_1 \ln(\tilde{R}_1) - 2\tilde{R}_1 \frac{S}{I_{-1}}, \tag{2.51}$$

with S from (2.32), as is given in Crowdy (2021). Determining the effective slip for the superposed annular flow is performed similarly. Equation (2.42) shows that the annular flow multiplied by β_2 (third term in brackets) does not contribute to λ_{eff}, since it is zero at the inner wall. Therefore,

$$\tilde{w}^* = \beta_1 \tilde{w}^*_{ca} = \beta_1 \tfrac{1}{4}(1 - \tilde{R}_1^2) + \beta_1 \tfrac{1}{2}(\tilde{R}_1^2 \ln(\tilde{R}_1) - MI_{-1} \ln(\tilde{R}_1)) \tag{2.52}$$

at $|\tilde{z}| = \tilde{R}_1$. From that, with (2.46), the effective slip length for the finite shear case is calculated easily to be

$$\tilde{\lambda}_{eff} = \frac{\lambda_{eff}}{R_0} = \tilde{R}_1 \ln(\tilde{R}_1) \, \beta_1 \frac{I_{-1} \ln(\tilde{R}_1) - 2S}{I_{-1} \ln(\tilde{R}_1) \, \beta_1 - 2S(\beta_1 - 1)}. \tag{2.53}$$

For $\beta_1 \to 1$, representing an infinite local slip length on the slit boundary parts, (2.53) converges to the effective slip length of the no-shear solution in (2.51), as expected.

3. Coupled flow – pipe within a pipe

Section 2 provides, among other things, analytical mathematical expressions for the pressure-driven flow field of a circular pipe flow (§ 2.1) and an annular pipe flow (§ 2.2), both containing a periodic array of longitudinal slits along one boundary. Both solutions presented stand for themselves. However, they assume not perfect slip, but rather a constant finite shear stress along these grooves, contrary to most of the literature (Lauga & Stone 2003; Sbragaglia & Prosperetti 2007; Crowdy 2016, 2021; Lee, Choi & Kim 2016; Yariv & Schnitzer 2018; Schnitzer & Yariv 2019). This is represented by a finite local slip
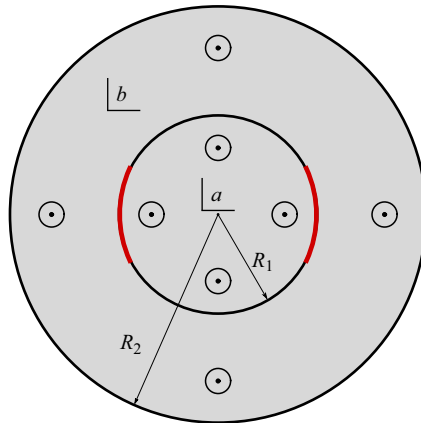
978 A20-12

Figure 3. Fluid domain connection: pipe flow (domain a) and annular flow (domain b) are connected via two rotationally symmetric shear slits on the inner wall, illustrated as bold red arcs.

length at the fluid–fluid interface, which is to be determined depending on the respective application. In the case of liquid-infused surfaces, this could be longitudinal grooves or other roughness features along the surface filled with a second immiscible fluid, usually air or oil. However, the practical application of such surfaces is challenging, as the trapped fluid can be pushed out of the microstructure. The interfacial collapse then leads to a Cassie–Wenzel transition. This ruins the desired effects of these surfaces, such as drag reduction. One way to prevent this is to use bottomless surfaces, where the downward walls inside the microstructures have been removed. This provides the operator with a greater degree of control. External pressure control, for example, can prevent the interface from collapsing. A possible configuration of such a surface is a pipe within a pipe, as illustrated in figure 3. Such a domain is composed of a pipe flow a and an annular flow b, which are connected along certain boundary areas, illustrated as red circular arcs in figure 3. This makes it possible, for example, to increase the interfacial stability by controlling both flow fields accordingly. Obviously, the pipe within a pipe geometry is composed of the solutions for the pipe flow and the annular flow derived in § 2, both of which have a local slip length as an unknown to be determined. These local slip lengths can be calculated readily as parameters depending on the corresponding linked flow field, so $\lambda_a = f(w_b)$ and vice versa. To emphasize that $\lambda_{a,b}$ follows from the connection of the two flow fields, it will be referred to here as $\Lambda_{a,b}$.

Accordingly, a pipe within a pipe is considered, connected through a periodic array of rotationally symmetric longitudinal slits on the outer wall of the inner circle. The no-slip wall portions of this boundary are assumed to be infinitely thin. Both domains are assumed to be pressure-driven and open downstream; accordingly, recirculation of the fluids is not considered. The outer radius of the governing equation of the inner pipe flow (2.13) is scaled to be of radius $\tilde{R}_1$, which corresponds to the inner radius of the annular flow solution. It is given by

$$w_a(\tilde{z}) = \frac{s_a R_0^2}{\mu_a} \left(\frac{1}{4} \, (\tilde{R}_1^2 - |\tilde{z}|^2) + \alpha(\tilde{\Lambda}_a) \, \frac{\tilde{R}_1^2}{N} \, \tau(\tilde{z}) \right), \tag{3.1}$$

with s_a, μ_a being the negative pressure gradient and viscosity within fluid domain a. The imperfection coefficient α is now defined in dependence on the normalized local connection slip length $\tilde{\Lambda}_a = \Lambda_a / R_0$ for the inner pipe. Here, R_0 is set to be the dimensional

radius of the outer pipe. The outer pipe flow is governed by the annular pipe flow solution of (2.39):

$$w_b(\tilde{z}) = \frac{1}{4} \frac{s_b R_0^2}{\mu_b} \left((1 - |\tilde{z}|^2) + 2\beta_1(\tilde{\Lambda}_b) \operatorname{Re}(H(\zeta)) - \beta_2(\tilde{\Lambda}_b) (1 - \tilde{R}_1^2) \frac{\ln(|\tilde{z}|)}{\ln(\tilde{R}_1)} \right), \quad (3.2)$$

with s_b, μ_b of domain b, and β_1, β_2 depending on the normalized local connection slip length $\tilde{\Lambda}_b = \Lambda_b/R_0$ for the outer pipe flow. A coupling of both flows has two unknowns, $\tilde{\Lambda}_a(w_b)$ and $\tilde{\Lambda}_b(w_a)$. Consequently, two connection conditions are needed. Specifically, both the velocity and shear stress at a single point on the interface must be equal, so

$$w_a(\tilde{\mathfrak{z}}) = w_b(\tilde{\mathfrak{z}}), \quad \mu_a \frac{\partial w_a(\tilde{\mathfrak{z}})}{-\partial \boldsymbol{n}} = -\mu_b \frac{\partial w_b(\tilde{\mathfrak{z}})}{\partial \boldsymbol{n}}, \quad (3.3a,b)$$

evaluated in the centre of the groove at $\tilde{\mathfrak{z}} = \tilde{R}_1 + \mathrm{i}0$. Solving the system of equations (3.3a,b) yields expressions for the local slip lengths

$$\tilde{\Lambda}_a(w_b) = \mu_a \Omega_a, \quad \tilde{\Lambda}_b(w_a) = \mu_b \Omega_b, \quad (3.4a,b)$$

where Ω_a, Ω_b are the connection coefficients of fluid domains a and b, respectively. They are given by

$$\Omega_a = -\frac{2\tilde{R}_1 \cosh^{-1}\left(\sec\left(\frac{\theta}{2}\right)\right)(\tilde{R}_1^2 - 2\operatorname{Re}(H(q)) - 1)\left((\tilde{R}_1^2 - 1)s_b + 2\tilde{R}_1^2 \ln\left(\frac{1}{\tilde{R}_1}\right)(s_b - s_a)\right)}{\left(\tilde{R}_1^2 + 2\tilde{R}_1^2 \ln\left(\frac{1}{\tilde{R}_1}\right) - 1\right)\left(Ns_b\mu_a(\tilde{R}_1^2 - 2\operatorname{Re}(H(q)) - 1) + 4\tilde{R}_1^2 s_a\mu_b \cosh^{-1}\left(\sec\left(\frac{\theta}{2}\right)\right)\right)}, \quad (3.5)$$

and $\Omega_a = -\Omega_b$. Both coefficients are dependent only on already known quantities and can be evaluated easily. The local connection slip lengths are in proportion to the viscosities of both fluid domains.

Although unequal pressure gradients s_a, s_b are not excluded explicitly in (3.5), the original assumption to neglect additional flow-induced interface curvature is no longer valid if $s_a \gg s_b$ or $s_a \ll s_b$. However, these equations can be used to consider cases where the local pressure difference $\Delta s = |s_a - s_b|$ at the fluid–fluid interface is less than the Laplace pressure. In the special case $s_a = s_b$, the connection coefficients can be simplified to

$$\Omega_{a,s} = -\frac{2\tilde{R}_1 \cosh^{-1}\left(\sec\left(\frac{\theta}{2}\right)\right)(\tilde{R}_1^2 - 2\operatorname{Re}(H(q)) - 1)(\tilde{R}_1^2 - 1)}{\left(\tilde{R}_1^2 + 2\tilde{R}_1^2 \ln\left(\frac{1}{\tilde{R}_1}\right) - 1\right)\left(N\mu_a(\tilde{R}_1^2 - 2\operatorname{Re}(H(q)) - 1) + 4\tilde{R}_1^2\mu_b \cosh^{-1}\left(\sec\left(\frac{\theta}{2}\right)\right)\right)}, \quad (3.6)$$

where, again, $\Omega_{a,s} = -\Omega_{b,s}$. The subscript s indicates the same pressure gradient in both flow domains. With both connection coefficients at hand, the normalized local connection slip length for both flow domains can be determined easily, using (3.3a,b). An interesting special case occurs when the same fluid flows in the inner and outer pipes, again with
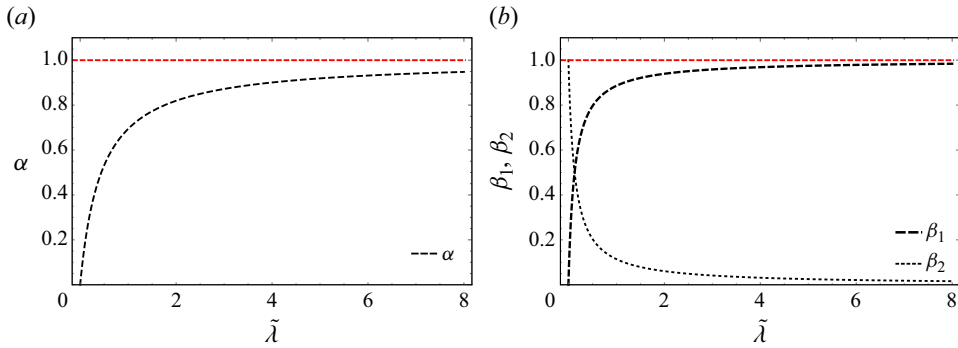
978 A20-14

Figure 4. Progression of imperfection and weighting coefficients with increasing local slip length $\tilde{\lambda}$ for $\theta = \pi/2$, $R_1 = 0.5$ and $N = 2$: (*a*) imperfectioncoefficient α; (*b*) weighting coefficients β_1 and β_2.

$s_a = s_b$. The coefficients simplify further and yield

$$
\tilde{\Lambda}_{a,s,\mu} = -\frac{2\tilde{R}_1 \cosh^{-1}\left(\sec\left(\dfrac{\theta}{2}\right)\right)(\tilde{R}_1^2 - 2\,\mathrm{Re}(H(q)) - 1)(\tilde{R}_1^2 - 1)}{\left(\tilde{R}_1^2 + 2\tilde{R}_1^2 \ln\left(\dfrac{1}{\tilde{R}_1}\right) - 1\right)\left(N(\tilde{R}_1^2 - 2\,\mathrm{Re}(H(q)) - 1) + 4\tilde{R}_1^2 \cosh^{-1}\left(\sec\left(\dfrac{\theta}{2}\right)\right)\right)},
$$

(3.7)

with $\tilde{\Lambda}_{a,s,\mu} = -\tilde{\Lambda}_{b,s,\mu}$. Index μ means that $\mu_a = \mu_b$.

4. Results and discussion

Sections 2 and 3 provide mathematical expressions for the flow field and the effective slip length for pipe and annular flow along rotationally symmetric longitudinal grooves, as well as their connection at the slit boundary parts, to model a pipe-within-pipe geometry. A flow through the aforementioned geometries is thus described fully as a function of the pipe radii, number of grooves and a maximum local (connection) slip length at the slit centre $\tilde{\mathfrak{z}}$.

4.1. *Imperfection and weighting coefficients*

Contrary to most of the literature, the solutions derived in this work have not necessarily an infinite local slip length at the slit boundary parts, but a potentially finite one. For $\theta = \pi/2$, radius $R_1 = 0.5$ and two slits, figure 4 illustrates the progression of the imperfection coefficient α of the superposed pipe flow (2.13) and the weighting coefficients β_1, β_2 of the superposed annular flow (2.39) with increasing local slip length. We consider only $\tilde{\lambda} \geq 0$. The dashed horizontal red line indicates the coefficient limit value 1.

With no local slip length at the boundary, $\alpha \to 0$, accordingly the second part of the superposed pipe flow determining the groove influence vanishes, leaving behind a Poiseuille flow with no slip at $|z| = R$. In contrast, the flow field at infinite slip length corresponds to the no-shear solution of Philip (1972*a*), since $\alpha \to 1$. For the superposed annular flow, β_1 and β_2 weight the influence of the no-shear solution provided by Crowdy (2021) and the superposed annular Poiseuille flow, respectively. For $\tilde{\lambda} = 0$, β_1 converges to 0 and β_2 converges to 1, accordingly (2.39) transitions into the annular Poiseuille flow with no-slip at $|z| = R_1$ and $|z| = R_2$. However, at infinite local slip lengths, we obtain the no-shear solution of Crowdy (2021), since $\beta_1 \to 1$ and $\beta_2 \to 0$, representing the

978 A20-15

ideal limit of a non-viscous interface interaction. As mentioned, the quantity of the local maximum slip length $\tilde{\lambda}$ is to be determined with respect to the system under consideration. The flow field of the pipe or annulus can therefore be calculated by specifying the local maximum slip length imposed by a microstructure, which is dependent on the properties of the enclosed fluid and the groove/structure geometry (Ybert *et al.* 2007; Schönecker *et al.* 2014).

4.2. *Flow fields for the pipe and annular flow*

For the pipe flow solution, examples of velocity contour lines are illustrated in figure 5. Figures 5(*a,c,e*) show contour plots of the axial velocity, assuming $N = 1, 2, 4$ no-shear slits along the pipe wall (red), at $|z| = R$. Figures 5(*b,d,f*) correspond to the same pipe geometries, but with finite local slip lengths along the grooves. It is easy to see that a finite slip length reduces the overall velocity of the flow compared to the no-shear solution, as expected. For $\tilde{\lambda} \to \infty$, figures 5(*b,d,f*) transition into figures 5(*a,c,e*), consequently corresponding to the ideal limit of non-viscous fluid–fluid interface interaction. Figure 6 shows contour plots of normalized pressure driven annular flow solutions, containing $N = 2, 3, 6$ slits (red) at $|z| = R_1$, and no-slip walls (blue) along the remaining boundaries. Whereas figures 6(*a,c,e*) assume no-shear grooves according to Crowdy's solution, figures 6(*b,d,f*) feature finite slip lengths.

4.3. *Connected flow field*

Now we will consider cases where the inner pipe flow is connected to the outer annular flow field, and vice versa. Figure 7 illustrates such a case for two slits, inner radius $R_1 = 0.5$ and $\theta = \pi/2$. In the present example, it is assumed that $\mu_a = \mu_b$ and $s_a = s_b$, which would correspond to the case of both pipe flows containing the same fluid and being driven by an equal pressure gradient. The analytically calculated coupled flow field is shown in figure 7(*a*). To verify the derived analytical solutions, numerical calculations have been performed with the commercial finite-element solver COMSOL Multiphysics®. For that, the two-dimensional Poisson equation has been solved for the inner and outer flow domains, as illustrated in figure 7(*b*). The fluid domains are connected at the red boundary parts. It should be noted that the mathematical connection of the flow fields in the numerical calculation is done along the complete fluid–fluid interface. In contrast, the analytical solution is coupled at only one point, the centre of the groove at coordinate $\tilde{\mathfrak{z}}$. The inner and outer no-slip walls (blue) impose $\tilde{w} = 0$ and are assumed to be infinitely thin, as is the assumption for the connected analytical flow field solution. The triangular mesh was refined strongly along the interface to resolve adequately the connection conditions, resulting in 374 752 mesh elements. Figure 7(*b*) shows the numerically calculated velocity contour plot. The comparison in figure 7 shows clearly the excellent agreement of both flow fields.

To investigate the agreement in more detail, a comparison of analytically and numerically calculated shear stresses, velocities and the corresponding local connection slip length distributions along the fluid–fluid interface is given in figure 8. All analytical solutions are based on the combined annular flow field of (3.2). Figures 8(*a,c,e*) examine a pipe-within-pipe flow regime for $N = 2$, $R_1 = 0.4$, $\theta = \pi/2$, and figures 8(*b,d,f*) for $N = 2$, $R_1 = 0.7$, $\theta = \pi/3$, assuming $\mu_a = \mu_b$ and $s_a = s_b$ in both cases. The underlying assumption of the derived analytical models is that the shear stress across the fluid–fluid interface is approximated to be constant. Such a condition has already been
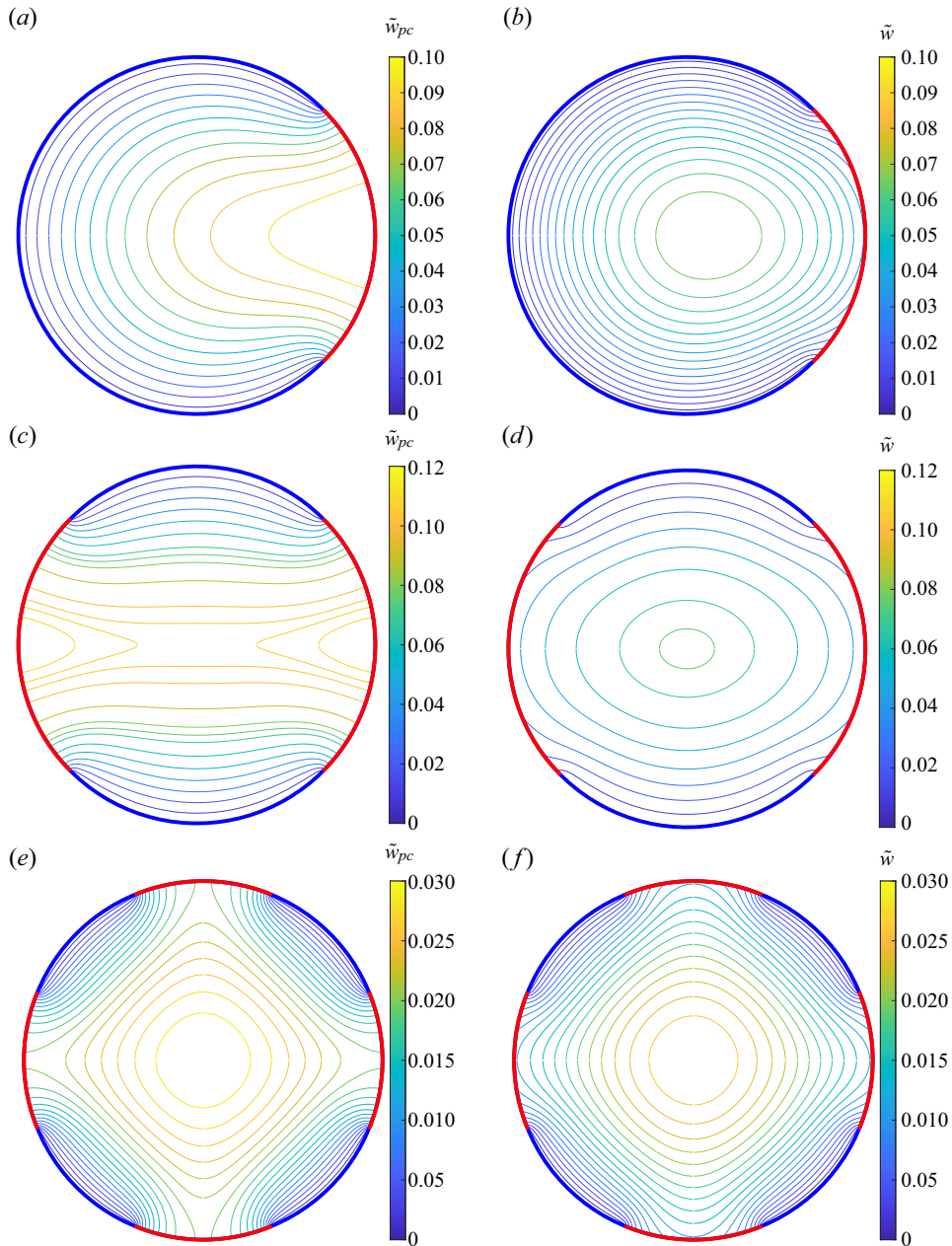
Figure 5. Variation of velocity contour lines through a pipe along rotationally symmetric slits (red) and no-slip boundaries (blue). Comparing no-shear (normalized (2.5)) with finite-shear (from (2.14)) solution. (*a*) No-shear slit: $N = 1$, $R = 0.5$, $\theta = \pi/4$. (*b*) Finite shear slit: as (*a*), with $\tilde{\lambda} = 0.2$. (*c*) No-shear slits: $N = 2$, $R = 0.5$, $\theta = \pi/2$. (*d*) Finite shear slits: as (*c*), with $\tilde{\lambda} = 0.2$. (*e*) No-shear slits: $N = 4$, $R = 0.3$, $\theta = \pi/2$. (*f*) Finite shear slits: as (*e*), with $\tilde{\lambda} = 0.2$.

used to describe finite-shear models, such as in Schönecker & Hardt (2013). Numerical simulations also show that the shear stress is indeed almost constant along the fluid–fluid interface (Higdon 1985; Schönecker *et al.* 2014), with merely small deviations at the corners. However, it should be mentioned that this assumption does not abolish the
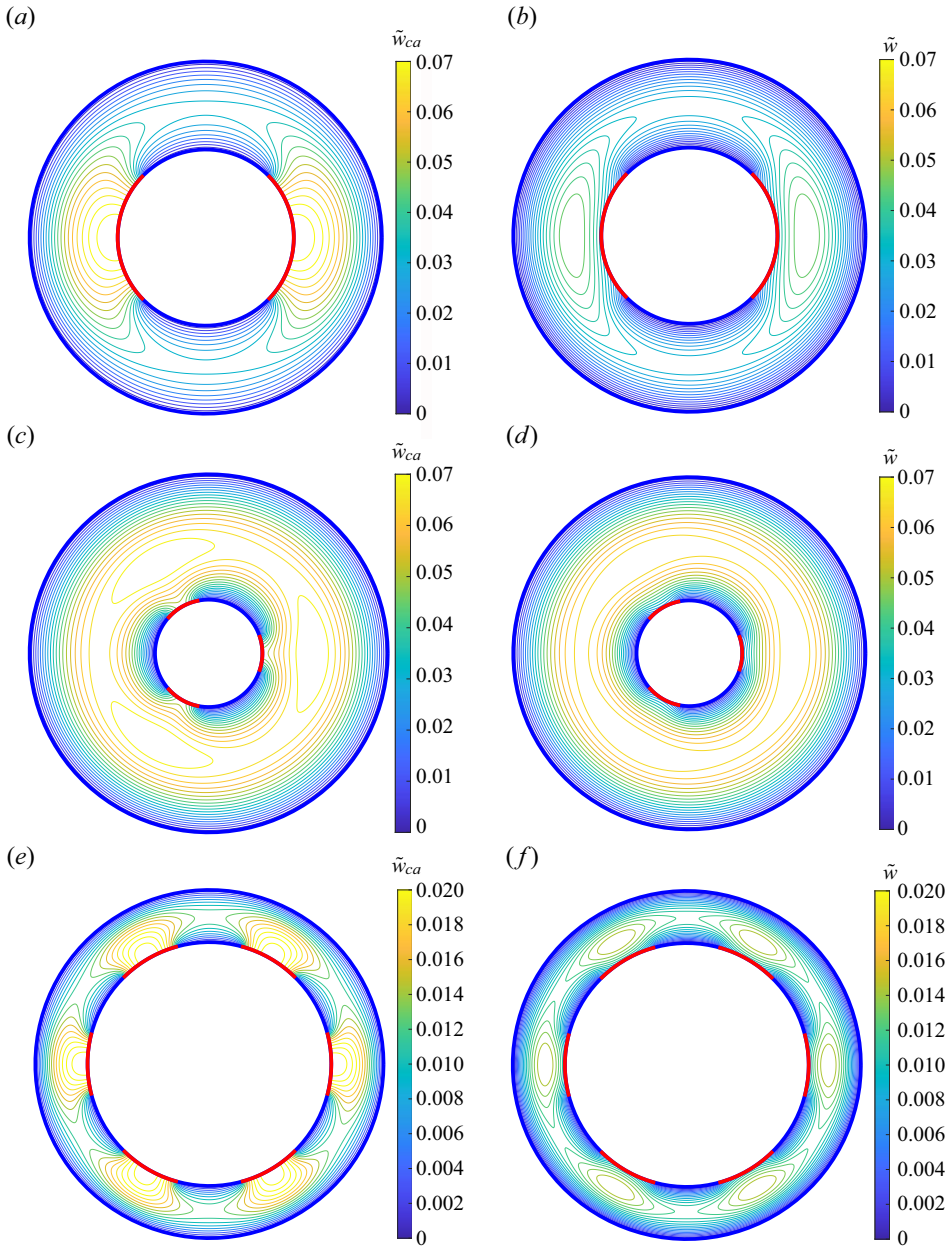
Figure 6. Variation of velocity contour lines through an annular pipe along rotationally symmetric slits (red) and no-slip boundaries (blue). Comparing no-shear (normalized (2.29)) with finite-shear (from (2.42)) solution. (*a*) No-shear slits: $N = 2$, $R = 0.5$, $\theta = \pi/2$. (*b*) Finite shear slits: as (*a*), with $\tilde{\lambda} = 0.2$. (*c*) No-shear slits: $N = 3$, $R = 0.3$, $\theta = \pi/3$. (*d*) Finite shear slits: as (*c*), with $\tilde{\lambda} = 0.1$. (*e*) No-shear slits: $N = 4$, $R = 0.7$, $\theta = \pi/2$. (*f*) Finite shear slits: as (*e*), with $\tilde{\lambda} = 0.1$.

singularities of the shear stress occurring in the transition to the solid wall, which are well captured by our model. Furthermore, the approach is closer to reality compared to the assumption of constant slip length along the interface, as the latter leads inevitably to slip length discontinuities at the groove corners. The numerical results from figures 8(*a*) and 8(*b*) show that the shear stress along the interface is not constant. The results differ

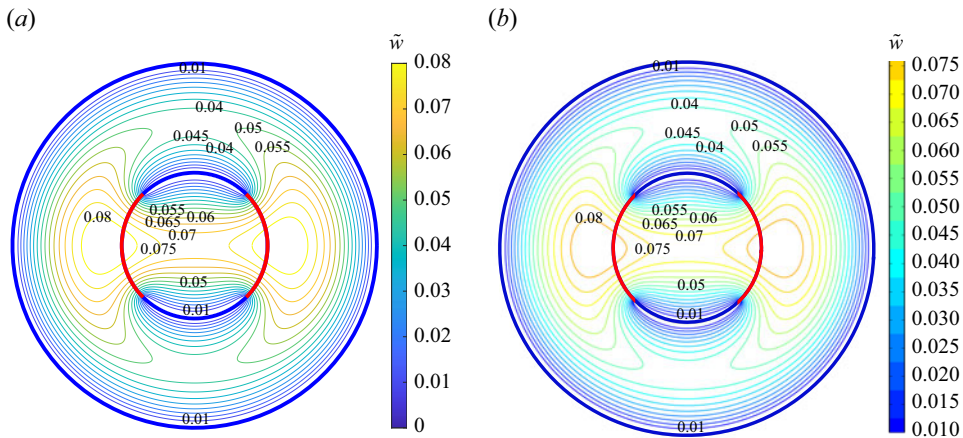(*a*)   (*b*)

Figure 7. Illustration of the normalized velocity contour lines with $N = 2$, $R = 0.4$ and $\theta = \pi/2$, assuming $\mu_a = \mu_b$ and $s_a = s_b$: (*a*) analytically calculated flow field from (3.1) and (3.2); (*b*) contour-lines calculated numerically are shown for comparison.

most at the corners of the grooves, as discussed above. Nevertheless, the comparison for both cases considered shows that the plots match remarkably well. This is especially remarkable since the largest deviations are to be expected along the interface anyway, which underlines further the quality of the assumption made. Analysing the averaged shear stress along the interfaces reveals further the cumulative error as being rather small, since $\Delta\tilde{\tau} = |\bar{\tilde{\tau}}_{num.} - \bar{\tilde{\tau}}_{ana.}| = 0.0377 - 0.0365 = 0.0012$ for figures 8(*a,c,e*), and $\Delta\tilde{\tau} = -0.159 - (-0.165) = 0.006$ for figures 8(*b,d,f*), with

$$\bar{\bar{\tau}} = \frac{1}{2\phi} \int_{-\phi}^{\phi} \tilde{\tau} \, d\phi, \tag{4.1}$$

where ϕ still is the slit half-angle. The difference can therefore be considered negligible, thus supporting our original assumption of constant shear.

The agreement between the numerical and analytical results for the normalized velocity along the interface is excellent, as can be seen in figures 8(*c,d*) for both geometries. Examining the plots for the local connection slip length distribution in figures 8(*e,f*), it is seen readily that the curves agree well. The discrepancy of the local connection slip length averaged over the interface

$$\overline{\tilde{\Lambda}} = \frac{1}{2\phi} \int_{-\phi}^{\phi} \tilde{\Lambda} \, d\phi \tag{4.2}$$

is $\Delta\tilde{\Lambda} = |\overline{\tilde{\Lambda}}_{num.} - \overline{\tilde{\Lambda}}_{ana.}| = 1.7710 - 1.820 = 0.049$ for figures 8(*a,c,e*), and $\Delta\tilde{\Lambda} = -0.350 - (-0.349) = 0.001$ for figures 8(*b,d,f*). The small observable deviations can be explained by the aforementioned assumption of constant shear stresses at the interface. However, considering the derived flow field solutions being the result of a superposition approach, the agreement is remarkable.

The previous consideration has been limited to the case $\mu_a = \mu_b$ and $s_a = s_b$. The interaction of air and water is shown in figure 9, but still with the same pressure gradient. Contour plots of the normalized axial velocities are illustrated, with both flow fields in a row being connected to each other. Each velocity is normalized with the corresponding viscosity of the associated domain, so $\tilde{w}_a = w_a(\mu_a/sR_0^2)$ and
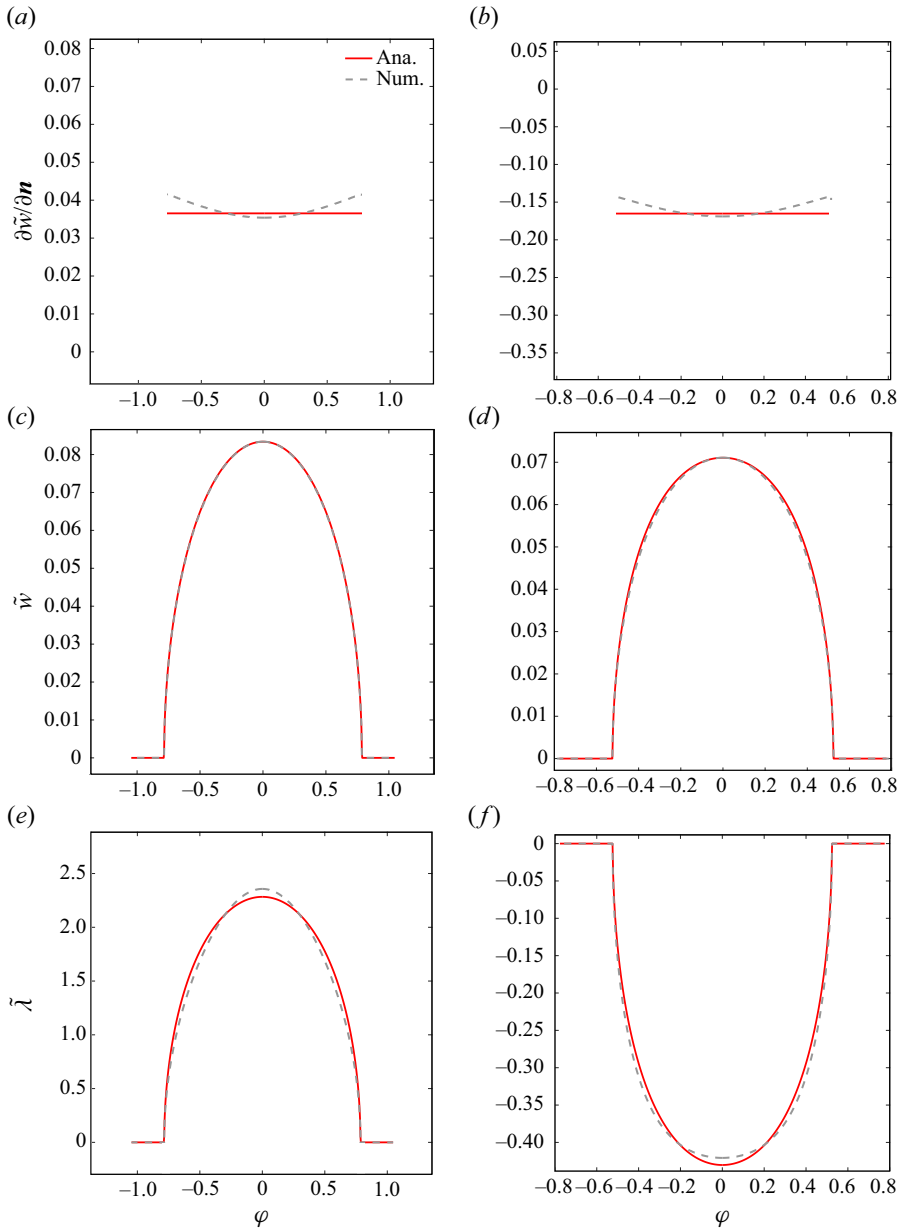
Figure 8. Comparison of results calculated analytically and numerically along the fluid–fluid interface at $\tilde{z} = R_1 \exp(i\varphi)$, with $\varphi \in [-\phi, \phi]$. The analytical solution is based on the combined annular flow field of (3.2): (a,c,e) $N = 2$, $R_1 = 0.4$ and $\theta = \pi/2$; (b,d,f) $N = 2$, $R_1 = 0.7$ and $\theta = \pi/3$. We assume $\mu_a = \mu_b$ and $s_a = s_b$ for both cases. (a,b) Normalized shear stresses; (c,d) normalized velocities; and (e,f) corresponding local connection slip length distributions.

$\tilde{w}_b = w_b(\mu_b/sR_0^2)$. Figures 9$(a,b)$ show an air flow ($\mu = 1.8 \times 10^{-5}$ Pa s) in the annular pipe connected to a pipe water flow ($\mu = 10^{-3}$ Pa s), with $N = 4$, $R_1 = 0.5$ and $\theta = \pi/4$. Although both flows have the same pressure gradient, it can be observed clearly that the air is accelerated comparatively strongly by the connection of the domains, resulting in
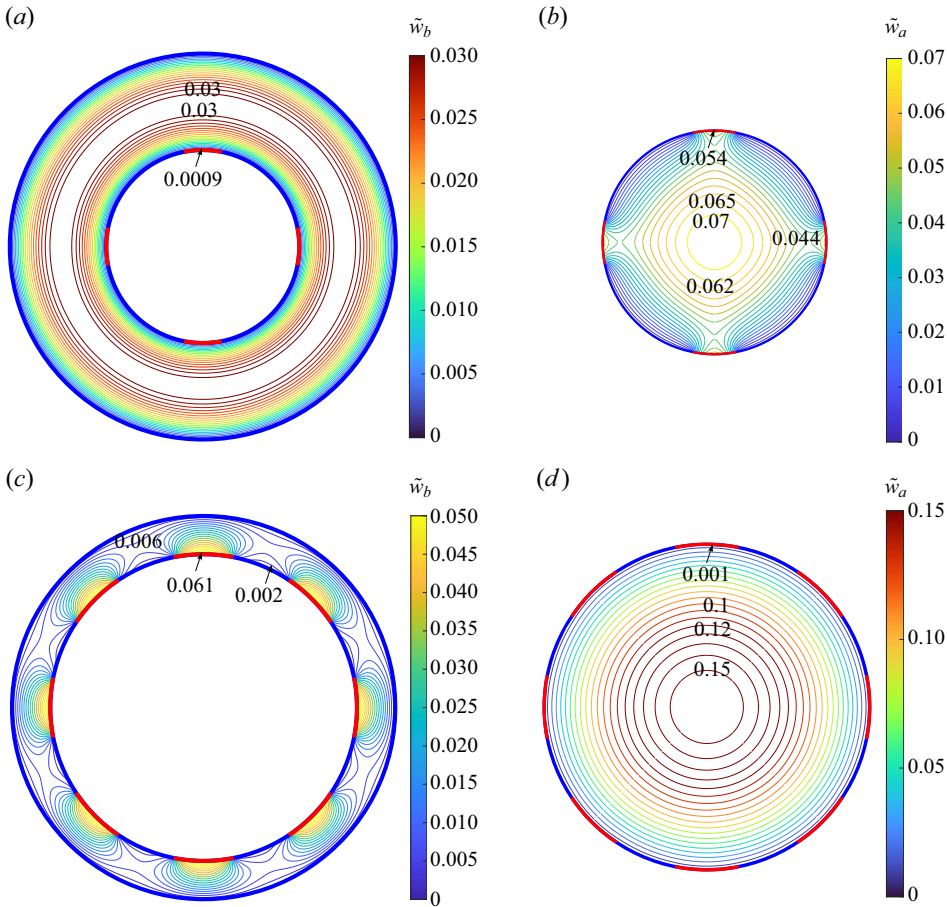
978 A20-20

Figure 9. Illustration of normalized flow field contour lines of a pipe flow (domain a) connected to an annular flow (domain b) with $\tilde{w}_a = w_a(\mu_a/sR_0^2)$ and $\tilde{w}_b = w_b(\mu_b/sR_0^2)$ for water ($\mu = 10^{-3}$ Pa s) and air ($\mu = 1.8 \times 10^{-5}$ Pa s). (a) Air flow through an annular pipe for $N = 4$, $R_1 = 0.5$ and $\theta = \pi/4$. (b) Water flow through a pipe connected to (a). (c) Water flow through an annular pipe for $N = 8$, $R_1 = 0.8$ and $\theta = \pi/2$. (d) Air flow through a pipe connected to (c).

an almost rotationally symmetrical velocity field in the annulus. While not immediately apparent, the velocities at the centre of each groove are equal, which can be verified easily by dividing by the viscosity. Figures 9(c,d) show the corresponding reverse case, with $N = 8$, $R_1 = 0.8$ and $\theta = \pi/2$. Again, the air now in the inner tube is disproportionately accelerated compared to the water in the annulus. Now, in figure 10, the interaction of water with oil ($\mu = 5 \times 10^{-3}$ Pa s) is illustrated, each with the same pressure gradient. The associated contour plots of the normalized velocities are illustrated, with both domains being connected at the centre of the red boundary parts ₃. Again, each velocity is normalized with the corresponding viscosity in its domain and both flow fields in a row being connected to each other. It should be noted that for better visibility, figures 10(b) and 10(d) are shown enlarged. Figures 10(a,b) consider a water flow in the outer pipe, oil correspondingly in the inner, with $N = 3$, $R_1 = 0.4$ and $\theta = \pi/3$. Figures 10(c,d) are unchanged geometrically, but the fluids are reversed.
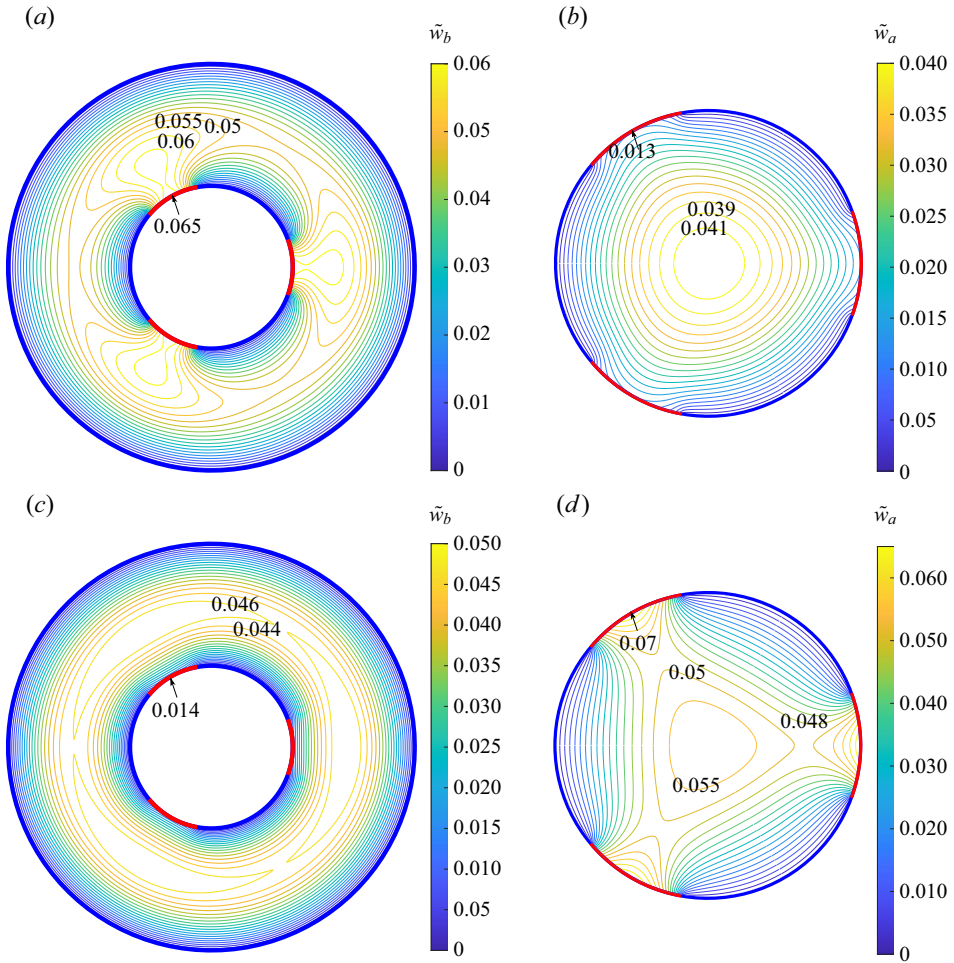
Figure 10. Illustration of normalized flow field contour lines of a pipe flow (domain *a*) connected to an annular flow (domain *b*) with $\tilde{w}_a = w_a(\mu_a/sR_0^2)$ and $\tilde{w}_b = w_b(\mu_b/sR_0^2)$ for water ($\mu = 10^{-3}$ Pa s) and oil ($\mu = 5 \times 10^{-3}$ Pa s). Note that for better visibility, (*b*,*d*) are shown enlarged. (*a*) Oil flow through an annular pipe for $N = 3$, $R_1 = 0.4$ and $\theta = \pi/3$. (*b*) Water flow through a pipe connected to (*a*). (*c*) Water flow through an annular pipe for $N = 3$, $R_1 = 0.4$ and $\theta = \pi/2$. (*b*) Oil flow through a pipe connected to (*a*).

4.4. *Local slip length for the connected case*

The local slip length $\tilde{\lambda}$ at the slit centre represents a certain, yet unknown, groove influence on the bulk pipe or annular flow and is to be determined accordingly. As discussed earlier, this depends on the fluid properties of the enclosed fluid as well as the microstructure geometry. Conventionally, confined grooves without their own pressure gradient are considered. This means that the bulk flow is not accelerated additionally by the groove, but merely slowed down less by the enclosed fluid that is passively dragged along compared to a solid no-slip wall. The considered velocity profile of the primary fluid then has a strictly positive normal derivative (normal vector points into the fluid zone by definition), as illustrated in figure 1. Assuming a velocity in the positive coordinate direction, the Navier-slip boundary condition dictates the local slip length to be defined as positive.
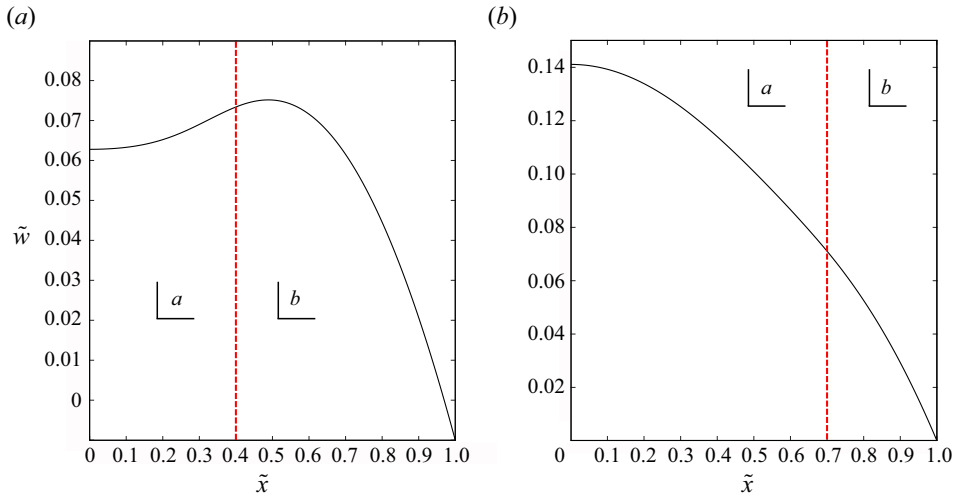
Figure 11. Change in the normalized axial velocity $\tilde{w}$ as $\tilde{z}$ traverses along the real axis from the centre of the pipe (region a) at $\tilde{z} = 0 + i0$ to the outer no-slip wall in the annular domain (region b) at $\tilde{z} = 1 + i0$. The red dashed line marks the transition between the two regions. The intersection of the curves marks the velocity in the centre of the interface $\tilde{z} = \tilde{\mathfrak{z}}$, assuming $\mu_a = \mu_b$ and $s_a = s_b$: (a) $N = 2$, $R_1 = 0.4$ and $\theta = \pi/2$; (b) $N = 2$, $R_1 = 0.7$ and $\theta = \pi/3$.

The linked pipe-within-pipe scenario is more general than this classical consideration. In the following, by linking the derived pipe flow and annular flow solution of § 2, mathematical expressions for $\tilde{\Lambda}_a(w_b)$ and $\tilde{\Lambda}_b(w_a)$ are obtained. The local connection slip lengths result intrinsically as a function of both individually pressure-driven linked flow fields. Both flow regimes can thus experience a sliding effect as well as an added acceleration effect at the fluid–fluid interface due to an additional pressure gradient in the other fluid zone. From the perspective of one fluid regime, it is now possible that a higher axial velocity exists beyond the interface. This is obviously not possible with purely shear-driven grooves. Following the previous notation, region a denotes the inner pipe flow, and region b the outer annular flow. Figure 11 shows two examples for the velocity in the $\tilde{Z}$-direction as one walks along the real axis, starting from the centre of the inner tube to the outer no-slip wall of the annulus. The red dashed line marks the transition between the two regions, i.e. the interface. When examining the velocity normal gradient at the interface, there are two cases to distinguish. Considering the condition (3.3b), either

$$\frac{\partial w_a(\tilde{\mathfrak{z}})}{-\partial \boldsymbol{n}} = -\frac{\partial w_b(\tilde{\mathfrak{z}})}{\partial \boldsymbol{n}} \quad \text{or} \quad \frac{\partial w_a(\tilde{\mathfrak{z}})}{-\partial \boldsymbol{n}} = \frac{\partial w_b(\tilde{\mathfrak{z}})}{\partial \boldsymbol{n}}. \tag{4.3a,b}$$

The first case follows from the fact that the velocity gradient of the inner pipe flow is defined in the negative radial coordinate direction, contrary to the annular flow part. This means that the normal derivative must always have different signs in the two fluid zones. This becomes evident when looking at e.g. figure 11(a). The local derivative of the axial velocity profile at the interface of the inner flow is negative as the profile decreases, since the derivative is defined in the negative x-direction ($\partial \tilde{w}/-\partial x$). In contrast, the derivative is positive for the outer flow, since the velocity still increases until reaching a maximum at $\tilde{x} \approx 0.5$. The exact opposite signs arise when considering the case of figure 11(b).

On the other hand, (4.3b) occurs only when both velocity gradients are equal at the interface, meaning that both must be zero, and it therefore must be an inflection point of the

axial velocity gradient function. Hence the shear stress at the interface is also zero. Locally, this corresponds to the no-shear solution derived by Philip (1972a) and Crowdy (2021). Such a case corresponds to a special case that can be brought about by the appropriate choice of geometry, fluid properties and/or pressure gradients.

It should be noted that potentially, the derived formulas of § 3 can result in negative local connection slip lengths. This is somewhat unintuitive at first. To clarify, let us consider the Navier-slip condition at the slit centre of the case illustrated in figure 11(a). As established, the velocity profile of the inner pipe flow has a local negative normal derivative at the interface, and the outer annular flow has a positive one. At the interface, the following must apply:

$$\tilde{\Lambda}_a \underbrace{\frac{\partial w_a(\tilde{\mathfrak{z}})}{-\partial \boldsymbol{n}}}_{<0} = \tilde{\Lambda}_b \underbrace{\frac{\partial w_b(\tilde{\mathfrak{z}})}{\partial \boldsymbol{n}}}_{>0}. \tag{4.4}$$

Since $w_a(\tilde{\mathfrak{z}}) = w_b(\tilde{\mathfrak{z}})$ must be true at the interface, the local connection slip lengths must correspond accordingly, indicating $\tilde{\Lambda}_a < 0$ and $\tilde{\Lambda}_b > 0$, if $w(\mathfrak{z}) > 0$. In the present example, $\tilde{\Lambda}_a < 0$ thus ensures that the direction of the axial velocity of the internal pipe flow at the interface is in the positive $\tilde{Z}$-direction. Additionally, negative connection slip lengths can lead to $\alpha(\tilde{\Lambda}) > 1$. This follows from the simple observation that a flow is driven by the pressure gradient of the linked flow in addition to its own pressure gradient, surpassing the effect of a no-shear boundary. One example would be pipe flow illustrated in figure 10(d), with $\alpha(\tilde{\Lambda}) = 2.34496$.

The weighting coefficients of the connected annular flow, on the other hand, can additionally be negative. However, this does not result in reverse flow, but may even exceed the case of no-shear slits, which will be shown in the following example. We consider $R_1 = 0.4$, $\theta = \pi/3$ and $N = 3$. The inner pipe has water ($\mu_a = 0.001$ Pa s) and the annular pipe oil ($\mu_b = 0.005$ Pa s) flowing through them, further assuming $s_1 = s_2$. The weighting coefficients of the annular flow field result to $\beta_1 = 1.30142$ and $\beta_1 = -0.30142$, accordingly. The associated flow field is shown in figure 10(a). By comparing the velocity in the centre of the slits, it can be shown that the present shear example has overall higher velocities than the comparison no-shear solution, since $\tilde{w}(\tilde{\mathfrak{z}}) = 0.065$ and $\tilde{w}_{ca}(\tilde{\mathfrak{z}}) = 0.049$.

5. Conclusions

This paper is concerned with modelling pressure-driven pipe flows along longitudinal slits or ridges filled with a second immiscible fluid. In addition to the classical pipe geometry, flow through an annulus containing grooves on its inner wall is also considered. Such flows have numerous applications, including water flowing over superhydrophobic surfaces or along porous media. Surfaces of this type can lead to a significant reduction of flow resistance and are therefore of great importance for the design of energy-efficient technical surfaces. The basis for the corresponding design process is the knowledge of the prevailing flow conditions in the immediate vicinity of the aforementioned microstructures and their consequential influence on the bulk flow. Analytical solutions can decipher this complex dynamics and are therefore of fundamental importance.

With a superposition technique, analytical approximations for the velocity field of longitudinal flow over rotationally symmetric microstructures in pipes (see (2.14)) and annuli (see (2.42)) were developed. The novelty of these solutions is their dependence on a finite local slip length evaluated at the centre of the fluid–fluid interface. This

contrasts with previous solutions by Philip (1972*a*) and Crowdy (2021). Typical solutions to these mixed value boundary problems assume perfect interfacial slip, corresponding to an infinite local slip length. This assumption represents an ideal limit of such interface interactions. The extension of these existing approaches performed in this paper now allows to factor in the actual influence of individual microstructures. It is not restricted whether the surface texture is closed or open (i.e. recirculation or not), whether it is a groove or another type of roughness feature. However, the prerequisite is the possibility of abstracting the influence by a local slip length at the slit centre.

Therefore, viscous interaction along the fluid–fluid interface and flow properties of the enclosed fluid, as well as the groove geometry, are now taken into account. With the analytical solutions now available, the flow field within a pipe or an annulus can be calculated fully as a function of rotationally symmetric longitudinal textures. The only prerequisite is knowledge of the local slip length at the centre of the interface, which remains to be determined on a case-specific basis. The equations are valid for single- and multi-phase flow. From these solutions, analytical expressions for the effective slip lengths are determined, which are an important building block in the numerical investigation of superhydrophobic walls.

The solutions derived in § 2 are important fundamental equations for the calculation of slippery pipes. However, a combination of those results leads to an interesting extension, a pipe-within-pipe geometry (discussed in § 3). For that, the pipe and annulus solutions are re-scaled and connected along their interfaces (see figure 3). This yields two interconnected flow regimes whose physical interfacial communication is modelled using local slip lengths as connection coefficients. Such a pipe-within-pipe promises greater operational control over the slippery effects, as unwanted interface protrusion and potential collapse can be prevented by appropriate external pressure control. The solutions derived in § 3 are determined fully, i.e. no longer dependent on still unknown local slip lengths. In fact, these are specified in the connection of both flow regions in dependence of the respective other flow. The resulting flow field equation is then only a function of fluid properties and geometry parameters, and therefore easily calculated.

Overall, a comparison of the analytical solutions with numerical simulations shows excellent agreement. This is particularly remarkable since the derived equations are the result of a comparatively simple superposition approach. This underlines strongly the validity and quality of the mathematical assumption of constant shear stress along all interfaces for such geometries. Ultimately, the presented equations enable further investigation on case-specific optimization of slippage along microstructured pipe walls.

Declaration of interests. The authors report no conflict of interest.

Author ORCIDs.
Clarissa Schönecker https://orcid.org/0000-0003-1826-9801.

REFERENCES

AGBE, H., SARKAR, D.K. & CHEN, X.G. 2020 Tunable superhydrophobic aluminum surfaces with anti-biofouling and antibacterial properties. *Coatings* **10** (10), 982.

ASMOLOV, E.S., NIZKAYA, T.V. & VINOGRADOVA, O.I. 2018 Enhanced slip properties of lubricant-infused grooves. *Phys. Rev.* E **98** (3), 033103.

BELYAEV, A.V. & VINOGRADOVA, O.I. 2010 Effective slip in pressure-driven flow past super-hydrophobic stripes. *J. Fluid Mech.* **652**, 489–499.

BOLOGNESI, G., COTTIN-BIZONNE, C. & PIRAT, C. 2014 Evidence of slippage breakdown for a superhydrophobic microchannel. *Phys. Fluids* **26** (8), 082004.

BUSSE, A., SANDHAM, N.D., MCHALE, G. & NEWTON, M.I. 2013 Change in drag, apparent slip and optimum air layer thickness for laminar flow over an idealised superhydrophobic surface. *J. Fluid Mech.* **727**, 488–508.

CAO, L., JONES, A.K., SIKKA, V.K., WU, J. & GAO, D. 2009 Anti-icing superhydrophobic coatings. *Langmuir* **25** (21), 12444–12448.

CASSIE, A.B.D. & BAXTER, S. 1944 Wettability of porous surfaces. *Trans. Faraday Soc.* **40**, 546–551.

CROWDY, D.G. 2016 Analytical formulae for longitudinal slip lengths over unidirectional superhydrophobic surfaces with curved menisci. *J. Fluid Mech.* **791**, R7.

CROWDY, D.G. 2020 *Solving Problems in Multiply Connected Domains*. SIAM.

CROWDY, D.G. 2021 Superhydrophobic annular pipes: a theoretical study. *J. Fluid Mech.* **906**, A15.

EPSTEIN, A.K., WONG, T.-S., BELISLE, R.A., BOGGS, E.M. & AIZENBERG, J. 2012 Liquid-infused structured surfaces with exceptional anti-biofouling performance. *Proc. Natl Acad. Sci. USA* **109** (33), 13182–13187.

HARDT, S. & MCHALE, G. 2022 Flow and drop transport along liquid-infused surfaces. *Annu. Rev. Fluid Mech.* **54**, 83–104.

HIGDON, J.J.L. 1985 Stokes flow in arbitrary two-dimensional domains: shear flow over ridges and cavities. *J. Fluid Mech.* **159**, 195–226.

KARATAY, E., HAASE, A.S., VISSER, C.W., SUN, C., LOHSE, D., TSAI, P.A. & LAMMERTINK, R.G.H. 2013 Control of slippage with tunable bubble mattresses. *Proc. Natl Acad. Sci. USA* **110** (21), 8422–8426.

KOCH, K., BHUSHAN, B. & BARTHLOTT, W. 2009 Multifunctional surface structures of plants: an inspiration for biomimetics. *Prog. Mater. Sci.* **54** (2), 137–178.

LATTHE, S.S., SUTAR, R.S., BHOSALE, A.K., NAGAPPAN, S., HA, C.-S., SADASIVUNI, K.K., LIU, S. & XING, R. 2019 Recent developments in air-trapped superhydrophobic and liquid-infused slippery surfaces for anti-icing application. *Prog. Org. Coat.* **137**, 105373.

LAUGA, E., BRENNER, M.P. & STONE, H.A. 2005 Microfluidics: the no-slip boundary condition. In *Handbook of Experimental Fluid Dynamics* (ed. J. Foss, C. Tropea & A. Yarin). Springer.

LAUGA, E. & STONE, H.A. 2003 Effective slip in pressure-driven Stokes flow. *J. Fluid Mech.* **489**, 55–77.

LEE, C., CHOI, C.-H. & KIM, C.-J. 2016 Superhydrophobic drag reduction in laminar flows: a critical review. *Exp. Fluids* **57** (12), 1–20.

MCHALE, G., FLYNN, M.R. & NEWTON, M.I. 2011 Plastron induced drag reduction and increased slip on a superhydrophobic sphere. *Soft Matt.* **7** (21), 10100–10107.

NIZKAYA, T.V., ASMOLOV, E.S. & VINOGRADOVA, O.I. 2014 Gas cushion model and hydrodynamic boundary conditions for superhydrophobic textures. *Phys. Rev.* E **90** (4), 043017.

OU, J., PEROT, B. & ROTHSTEIN, J.P. 2004 Laminar drag reduction in microchannels using ultrahydrophobic surfaces. *Phys. Fluids* **16** (12), 4635–4643.

PHILIP, J.R. 1972*a* Flows satisfying mixed no-slip and no-shear conditions. *Z. Angew. Math. Phys.* **23** (3), 353–372.

PHILIP, J.R. 1972*b* Integral properties of flows satisfying mixed no-slip and no-shear conditions. *Z. Angew. Math. Phys.* **23** (6), 960–968.

RAS, R.H. & MARMUR, A. 2016 *Non-Wettable Surfaces: Theory, Preparation and Applications*. Royal Society of Chemistry.

ROTHSTEIN, J.P. 2010 Slip on superhydrophobic surfaces. *Annu. Rev. Fluid Mech.* **42**, 89–109.

SBRAGAGLIA, M. & PROSPERETTI, A. 2007 A note on the effective slip properties for microchannel flows with ultrahydrophobic surfaces. *Phys. Fluids* **19** (4), 043603.

SCHÄFFEL, D., KOYNOV, K., VOLLMER, D., BUTT, H.-J. & SCHÖNECKER, C. 2016 Local flow field and slip length of superhydrophobic surfaces. *Phys. Rev. Lett.* **116** (13), 134501.

SCHNITZER, O. & YARIV, E. 2019 Stokes resistance of a solid cylinder near a superhydrophobic surface. Part 1. Grooves perpendicular to cylinder axis. *J. Fluid Mech.* **868**, 212–243.

SCHÖNECKER, C., BAIER, T. & HARDT, S. 2014 Influence of the enclosed fluid on the flow over a microstructured surface in the Cassie state. *J. Fluid Mech.* **740**, 168–195.

SCHÖNECKER, C. & HARDT, S. 2013 Longitudinal and transverse flow over a cavity containing a second immiscible fluid. *J. Fluid Mech.* **717**, 376–394.

SCHÖNECKER, C. & HARDT, S. 2015 Assessment of drag reduction at slippery, topographically structured surfaces. *Microfluid Nanofluid* **19** (1), 199–207.

SHIRTCLIFFE, N.J., MCHALE, G., ATHERTON, S. & NEWTON, M.I. 2010 An introduction to superhydrophobicity. *Adv. Colloid Interface Sci.* **161** (1–2), 124–138.

VINOGRADOVA, O.I. 1999 Slippage of water over hydrophobic surfaces. *Intl J. Miner. Process.* **56** (1–4), 31–60.

WENZEL, R.N. 1936 Resistance of solid surfaces to wetting by water. *Ind. Engng Chem.* **28** (8), 988–994.

WONG, T., KANG, S.H., TANG, S.K.Y., SMYTHE, E.J., HATTON, B.D., GRINTHAL, A. & AIZENBERG, J. 2011 Bioinspired self-repairing slippery surfaces with pressure-stable omniphobicity. *Nature* **477** (7365), 443–447.

YARIV, E. & SCHNITZER, O. 2018 Pressure-driven plug flows between superhydrophobic surfaces of closely spaced circular bubbles. *J. Engng Maths* **111** (1), 15–22.

YBERT, C., BARENTIN, C., COTTIN-BIZONNE, C., JOSEPH, P. & BOCQUET, L. 2007 Achieving large slip with superhydrophobic surfaces: scaling laws for generic geometries. *Phys. Fluids* **19** (12), 123601.